

IEEE

# GEOSCIENCE AND REMOTE SENSING LETTERS

A PUBLICATION OF THE IEEE GEOSCIENCE AND REMOTE SENSING SOCIETY



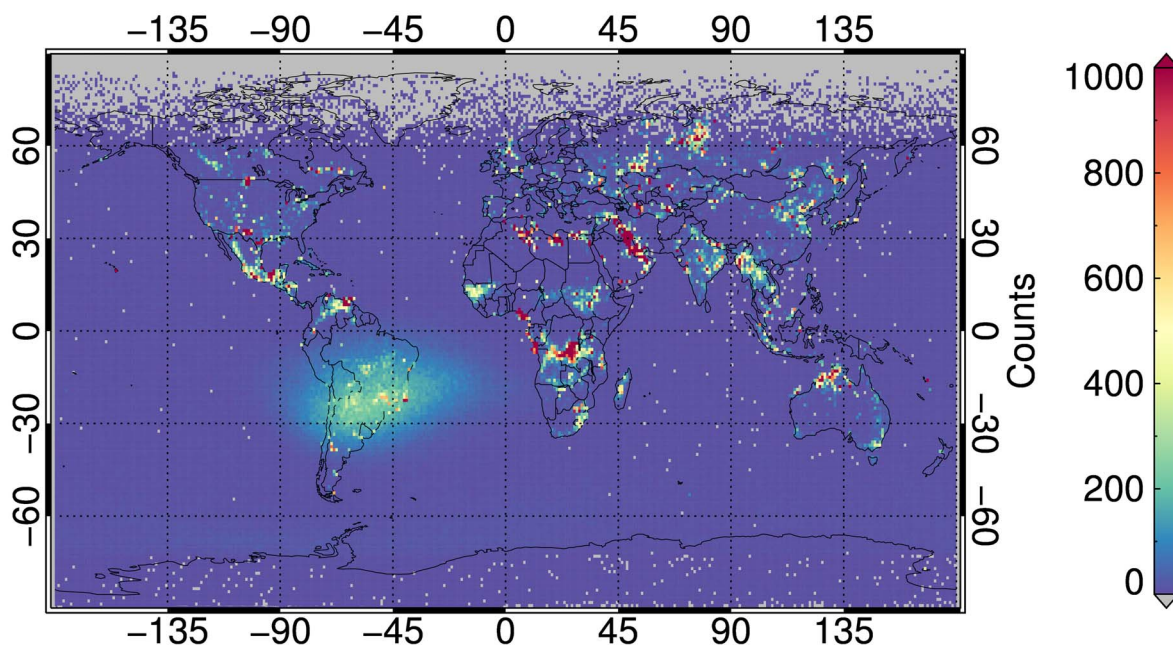
JUNE 2015

VOLUME 12

NUMBER 6

IGRSBY

(ISSN 1545-598X)



Regions of frequent biomass burning and gas flaring highlighted by NOAA's Nightfire product during 18 March–14 July 2013. Interference from the South Atlantic Anomaly (SAA) is visible over a large portion of South America.

IEEE

# GEOSCIENCE AND REMOTE SENSING LETTERS

A PUBLICATION OF THE IEEE GEOSCIENCE AND REMOTE SENSING SOCIETY



JUNE 2015

VOLUME 12

NUMBER 6

IGRSBY

(ISSN 1545-598X)

## EDITORIAL

How To Successfully Make a Scientific Contribution Through IEEE Geoscience and Remote Sensing Letters . . . . .	A. C. Frery	1167
---	-------------	------

## PAPERS

### Atmosphere

Scanning Strategy for the Multifunction Phased-Array Radar to Satisfy Aviation and Meteorological Needs . . . . .	<i>D. S. Zrnic, V. M. Melnikov, R. J. Doviak, and R. Palmer</i>	1204
Accurate Aerial Object Localization Using Gravity and Gravity Gradient Anomaly . . . . .	<i>Z. Yan, J. Ma, and J. Tian</i>	1214
Enhancing the Detectability of Clouds and Their Shadows in Multitemporal Dryland Landsat Imagery: Extending Fmask . . . . .	<i>D. Frantz, A. Röder, T. Udelhoven, and M. Schmidt</i>	1242
<b>First Global Analysis of Saturation Artifacts in the VIIRS Infrared Channels and the Effects of Sample Aggregation</b> . . . . .	<i>T. N. Polivka, E. J. Hyer, J. Wang, and D. A. Peterson</i>	1262
Observation of Polar Mesospheric Clouds by Geostationary Satellite Sensors . . . . .	<i>S. Proud</i>	1332
Ground-Based Cloud Detection Using Automatic Graph Cut . . . . .	<i>S. Liu, Z. Zhang, B. Xiao, and X. Cao</i>	1342

### Oceans and Water

Influence of Particle Composition on Remote Sensing Reflectance and MERIS Maximum Chlorophyll Index Algorithm: Examples From Taihu Lake and Chaohu Lake . . . . .	<i>L. Qi, C. Hu, H. Duan, Y. Zhang, and R. Ma</i>	1170
Measurements of the Cross-Loop Antenna Patterns in High-Frequency Surface Wave Radars . . . . .	<i>X. Shi, X. Xu, Z. Shi, and Z. Tang</i>	1272
Evaluation of Aquarius Sea Surface Salinity With Argo Sea Surface Salinity in the Tropical Indian Ocean . . . . .	<i>T. V. S. U. Bhaskar and C. Jayaram</i>	1292

### Vegetation and Land Surface

Estimation of Fractional Vegetation Cover in Semiarid Areas by Integrating Endmember Reflectance Purification Into Nonlinear Spectral Mixture Analysis . . . . .	<i>L. Ma, Y. Zhou, J. Chen, X. Cao, and X. Chen</i>	1175
Performance Evaluation of Semantic Kriging: A Euclidean Vector Analysis Approach . . . . .	<i>S. Bhattacharjee and S. K. Ghosh</i>	1185
Validity Regions of Soil Moisture Retrieval on the LAI- $\theta$ Plane for Agricultural Fields at L-, C-, and X-Bands. . . . .	<i>S. Park, S.-K. Kweon, and Y. Oh</i>	1195

(Contents Continued on Page 1166)



---

Rice Growth Monitoring by Means of X-Band Co-polar SAR: Feature Clustering and BBCH Scale . . . . .	1218
. . . . . <i>O. Yuzugullu, E. Erten, and I. Hajnsek</i>	
The Impact of Temporal Decorrelation on BIOMASS Tomography of Tropical Forests . . . . .	1297
. . . . . <i>D. Ho Tong Minh, S. Tebaldini, F. Rocca, and T. Le Toan</i>	
<b>Surface and Subsurface Properties</b>	
Three-Dimensional Cole-Cole Model Inversion of Induced Polarization Data Based on Regularized Conjugate Gradient Method . . . . .	1180
. . . . . <i>Z. Xu and M. S. Zhdanov</i>	
Adaptive Time–Frequency Peak Filtering Based on Convex Sets and the Viterbi Algorithm . . . . .	1267
. . . . . <i>Q. Zeng, Y. Li, and X. Deng</i>	
Application of Linear Predictive Coding for Doppler Through-Wall Radar Target Tracking . . . . .	1317
. . . . . <i>Y. Ding, J. Tang, X. Xu, and J. Zhang</i>	
Rock Surface Classification in a Mine Drift Using Multiscale Geometric Features . . . . .	1322
. . . . . <i>G. Mills and G. Fotopoulos</i>	
Adaptive Differential Evolution by Adjusting Subcomponent Crossover Rate for High-Dimensional Waveform Inversion . . . . .	1327
. . . . . <i>Z. Pan, J. Wu, Z. Gao, and J. Gao</i>	
Sidewall Detection Using Multipath in Through-Wall Radar Moving Target Tracking . . . . .	1372
. . . . . <i>J. Liu, G. Cui, Y. Jia, L. Kong, and X. Yang</i>	
<b>Image Processing, Analysis, and Classification</b>	
Built-Up Area Detection From Satellite Images Using Multikernel Learning, Multifield Integrating, and Multihypothesis Voting . . . . .	1190
. . . . . <i>Y. Li, Y. Tan, Y. Li, S. Qi, and J. Tian</i>	
Automatic Change Analysis in Satellite Images Using Binary Descriptors and Lloyd–Max Quantization . . . . .	1223
. . . . . <i>A. Radoi and M. Datcu</i>	
A Novel Image Classification Algorithm Using Overcomplete Wavelet Transforms . . . . .	1232
. . . . . <i>S. W. Myint, T. Zhu, and B. Zheng</i>	
Land-Cover Classification of Remotely Sensed Images Using Compressive Sensing Having Severe Scarcity of Labeled Patterns . . . . .	1257
. . . . . <i>M. Roy, F. Melgani, A. Ghosh, E. Blanzieri, and S. Ghosh</i>	
Circular Oil Tank Detection From Panchromatic Satellite Images: A New Automated Approach . . . . .	1347
. . . . . <i>A. O. Ok and E. Başeski</i>	
A Comparative Study of Bag-of-Words and Bag-of-Topics Models of EO Image Patches . . . . .	1357
. . . . . <i>R. Bahmanyar, S. Cui, and M. Datcu</i>	
Spatial and Temporal Image Fusion via Regularized Spatial Unmixing . . . . .	1362
. . . . . <i>Y. Xu, B. Huang, Y. Xu, K. Cao, C. Guo, and D. Meng</i>	
<b>Hyperspectral Data Processing</b>	
Fast and Reliable Noise Estimation for Hyperspectral Subspace Identification . . . . .	1199
. . . . . <i>P. Benner, V. Novaković, A. Plaza, E. S. Quintana-Ortí, and A. Remón</i>	
Hyperspectral Image Classification Using Weighted Joint Collaborative Representation . . . . .	1209
. . . . . <i>M. Xiong, Q. Ran, W. Li, J. Zou, and Q. Du</i>	
Nonlinear PCA for Visible and Thermal Hyperspectral Images Quality Enhancement . . . . .	1228
. . . . . <i>G. A. Licciardi and J. Chanussot</i>	
Informative Change Detection by Unmixing for Hyperspectral Images . . . . .	1252
. . . . . <i>A. Ertürk and A. Plaza</i>	
Kernel Fukunaga–Koontz Transform Subspaces for Classification of Hyperspectral Images With Small Sample Sizes . . . . .	1287
. . . . . <i>H. Binol, G. Bilgin, S. Dinc, and A. Bal</i>	
<b>Radar Systems</b>	
A Novel Radar Waveform Design for a Low-Power HF Monostatic Radar . . . . .	1352
. . . . . <i>S. Shi, G. Yang, Z. Zhao, and J. Liu</i>	
<b>Synthetic Aperture Radar</b>	
A MAP Approach for 1-Bit Compressive Sensing in Synthetic Aperture Radar Imaging . . . . .	1237
. . . . . <i>X. Dong and Y. Zhang</i>	
Target Recognition via Information Aggregation Through Dempster–Shafer’s Evidence Theory . . . . .	1247
. . . . . <i>G. Dong and G. Kuang</i>	
A Method for Detecting Buildings Destroyed by the 2011 Tohoku Earthquake and Tsunami Using Multitemporal TerraSAR-X Data . . . . .	1277
. . . . . <i>H. Gokon, J. Post, E. Stein, S. Martinis, A. Twele, M. Mück, C. Geiß, S. Koshimura, and M. Matsuoka</i>	
Performance Analysis of Phase Gradient Autofocus for Compensating Ionospheric Phase Scintillation in BIOMASS P-Band SAR Data . . . . .	1367
. . . . . <i>Z. Li, S. Quegan, J. Chen, and N. C. Rogers</i>	

---

---

A Novel Fast Approach for SAR Tomography: Two-Step Iterative Shrinkage/Thresholding . . . . .	<i>L. Wei, T. Balz, L. Zhang, and M. Liao</i>	1377
<b>Lidar Systems</b>		
An Improved Method for Transforming GPS/INS Attitude to National Map Projection Frame . . . . .	<i>X. Shen, Y. Zhang, X. Lu, Q. Xie, and Q. Li</i>	1302
<b>HIWATER Special Stream</b>		
Analysis and Reduction of the Uncertainties in Soil Moisture Estimation With the L-MEB Model Using EFAST and Ensemble Retrieval . . . . .	<i>D. Li, R. Jin, J. Zhou, and J. Kang</i>	1337
<b>EORSA 2014 Special Stream</b>		
An Automated Method to Parameterize Segmentation Scale by Enhancing Intra-segment Homogeneity and Inter-segment Heterogeneity . . . . .	<i>J. Yang, Y. He, and Q. Weng</i>	1282
Characterizing Crop Responses to Background Ozone in Open-Air Agricultural Field by Using Reflectance Spectroscopy . . . . .	<i>A. Ghulam, J. Fishman, M. Maimaitiyiming, J. L. Wilkins, M. Maimaitijiang, J. Welsh, B. Bira, and M. Grzovic</i>	1307
Evaluating the Operational Retrieval and Downscaling of Urban Land Surface Temperatures . . . . .	<i>P. Sismanidis, I. Keramitsoglou, and C. T. Kiranoudis</i>	1312
<hr/>		
ANNOUNCEMENTS		
Call for Papers—IEEE GEOSCIENCE AND REMOTE SENSING MAGAZINE . . . . .		1382

---

**About the Cover:** Global distribution of the Visible Infrared Imaging Radiometer Suite’s (VIIRS) 3.7- $\mu\text{m}$  fire pixel detections from NOAA’s Nightfire product during 18 March–14 July 2013. A high-frequency of detections (gridded to  $1^\circ \times 1^\circ$ ) is observed in regions that frequently burn biomass (Central Africa, Central America, Southeast Asia) and flare gas (Persian Gulf, North Dakota, and Nigeria). Volcanoes are also detected, such as on the Hawaiian and Aleutian Islands. Despite attempts to filter out sensor noise from the South Atlantic Anomaly (SAA), it is still present in the final Nightfire product and artificially inflates fire pixel detections over South America. The vast majority of low-density grid cells (purple shading) are false detections triggered by sensor noise. Gray areas indicate no detections. For more information please see “First Global Analysis of Saturation Artifacts in the VIIRS Infrared Channels and the Effects of Sample Aggregation,” by Polivka *et al.*, which begins on page 1262.

# First Global Analysis of Saturation Artifacts in the VIIRS Infrared Channels and the Effects of Sample Aggregation

Thomas N. Polivka, Edward J. Hyer, Jun Wang, and David A. Peterson

**Abstract**—Unlike previous spaceborne Earth observing sensors, the Visible Infrared Radiometer Suite (VIIRS) employs onboard sample aggregation to reduce downlink bandwidth requirements and preserve spatial resolution across the scan. To examine the potentially deleterious impacts of onboard sample aggregation when encountering detector saturation, nearly four months of the National Oceanic and Atmospheric Administration's Nightfire product are analyzed, which contains a subset of the hottest observed nighttime pixels. An empirical method for identifying saturation is devised. The M12 band (3.69  $\mu\text{m}$ ) is the most frequently saturating band with 0.15% of the Nightfire pixels at or near the  $\sim 359\text{-K}$  detector saturation limit; some saturation is also found in M14, M15, and M16 (8.58, 10.74, and 11.86  $\mu\text{m}$ ). Artifacts consistent with detector saturation are seen with M12 temperatures as low as 330 K in the scene center. This partial saturation and aggregation influence must be considered when using VIIRS radiances for quantitative characterization of hot emission sources such as fires and gas flaring.

**Index Terms**—Fires, infrared measurements, nightfire, remote sensing, sample aggregation, saturation, Suomi National Polar-orbiting Partnership (S-NPP), Visible Infrared Imaging Radiometer Suite (VIIRS).

## I. INTRODUCTION

ON October 28, 2011, the Suomi National Polar-orbiting Partnership (S-NPP) satellite was launched from the Vandenberg Air Force Base in California, and it now orbits with a mean altitude of 840 km above the Earth in sun-synchronous orbit. Located aboard S-NPP, the Visible Infrared Imaging Radiometer Suite (VIIRS) is a 22-band scanning radiometer with a nominal spatial resolution of 375 m in the five imagery bands (I-bands) and 750 m in both the 16 moderate-resolution bands (M-bands) and the day-night band (DNB) [1]–[4] (see Table I). The sensor data records (SDRs) of calibrated radiances and brightness temperatures cover a spectral range from 0.411

Manuscript received July 9, 2014; revised November 18, 2014; accepted December 28, 2014. Date of publication January 1, 2014; date of current version January 1, 2014. This work was supported by the University of Nebraska-Lincoln. The work of J. Wang was supported by the National Aeronautics and Space Administration (NASA) S-NPP Program and Applied Science Program under Grant NNX11AJ03G managed by John A. Haynes and Lawrence A. Friedl. T. Polivka also acknowledges the support from the NASA Nebraska Space Grant.

T. N. Polivka and J. Wang are with the Department of Earth and Atmospheric Sciences, University of Nebraska-Lincoln, Lincoln, NE 68588 USA (e-mail: thomas.polivka@huskers.unl.edu; jwang7@unl.edu).

E. J. Hyer is with the Marine Meteorology Division, Naval Research Laboratory, Monterey, CA 93943 USA (e-mail: edward.hyer@nrlmry.navy.mil).

D. A. Peterson is with the National Research Council, Monterey, CA 93943 USA (e-mail: david.peterson.ctr@nrlmry.navy.mil).

Digital Object Identifier 10.1109/LGRS.2015.2392098

TABLE I  
GENERAL SUOMI-NPP AND VIIRS SENSOR  
CHARACTERISTICS [1], [2], [10]

Launch date	28 October, 2011
Orbit description	Near-circular, near-polar, sun-synchronous
Mean orbital altitude	840 km
Inclination	98.7°
Orbital period	101.5 min.
Ascending equator local crossing time	13:30 $\pm$ 10 min.
Swath width	$\sim 3000$ km
Number of bands	5 I-bands, 16 M-bands, 1 DNB
Nominal spatial resolution	375 m (I-bands), 750 m (M-bands, DNB)
Spectral range	0.411–11.87 $\mu\text{m}$
Detectors per band	32 (I-bands), 16 (M-bands), 672 (DNB)
Lines per scan	32 (I-bands), 16 (M-bands, DNB)

to 11.87  $\mu\text{m}$  and are used in a wide range of Earth observation applications, including fire detection and characterization, retrieval of cloud and aerosol properties, and land and sea surface temperature estimation [5]. The VIIRS sensor was designed to improve upon legacy instruments, such as the Moderate Resolution Imaging Spectroradiometer (MODIS), the Advanced Very High Resolution Radiometer, and the Operational Line Scanner. One significant enhancement relative to these legacy sensors is that VIIRS does not experience the significant off-nadir pixel growth affecting sensors such as MODIS; VIIRS pixels at the scan edge are only two to four times the size of nadir pixels, whereas MODIS exhibits a growth factor of 10 [2]. For the M-bands, VIIRS delivers SDRs of calibrated radiances and brightness temperatures with a pixel instantaneous field of view (IFOV) of  $0.75 \times 0.79$  km at nadir, which increases to  $1.66 \times 1.71$  km at the edge of the scan [1], whereas the five imagery bands have smaller IFOVs ranging from  $0.38 \times 0.39$  km to  $0.83 \times 0.86$  km at the scan edge.

The spatial resolution of VIIRS is preserved across the scan by employing asymmetrical detectors in conjunction with a unique sample aggregation scheme, as illustrated in Fig. 1, which combines multiple samples from one rectangular detector into single raw data record (RDR) pixels consisting of digital counts. This processing is done onboard the satellite, except for the dual-gain bands whose aggregation is done on the ground [2]. As a result, the RDR has three aggregation zones. The 3:1 aggregation zone refers to scan angles between  $0^\circ$  (nadir) and  $31.72^\circ$ , where the value of each pixel is actually the average of three individual samples. Similarly, in the 2:1 aggregation zone (scanning angles between  $31.72^\circ$  and  $44.86^\circ$ ), two samples from the same detector are aggregated to form a pixel. No sample aggregation is performed in the

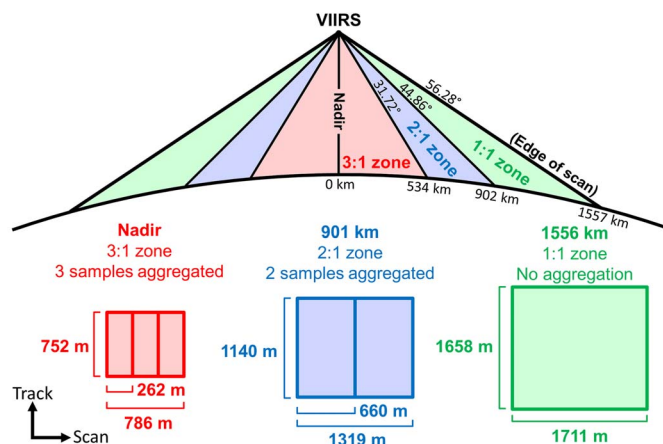


Fig. 1. VIIRS aggregation scheme (not to scale) and sample dimensions over the equator with an orbital altitude of 830 km [2]. The individual rectangles represent samples from an M-band detector, shaded by aggregation zone.

1:1 aggregation zone (scan angles greater than  $44.86^\circ$ ); thus, each pixel is calculated from a single detector sample. Once the RDR has been generated, it is later processed into a calibrated SDR, retaining the characteristics from aggregation.

While the VIIRS aggregation scheme effectively reduces pixel footprint growth across the scan, it also results in fundamental differences in the data characteristics among the three aggregation zones, particularly when detector saturation occurs. The VIIRS onboard electronics module does not flag the data if an individual sample saturates before aggregation occurs. Consequently, the aggregation of samples does not account for saturation effects, which may result in biases or artifacts for pixels containing active biomass burning or other heat sources that have the potential to cause detector saturation. In the case when an individual sample is saturated and then aggregated with unsaturated samples, the resulting pixel will have a radiance bias associated with saturation, even if the reported pixel radiance is well below the detector saturation limit. This study investigates the frequency and effects of saturated samples in the VIIRS infrared (IR) channels and evaluates the potential for biases and artifacts in the VIIRS SDR caused by onboard sample aggregation. This study represents a first attempt to derive an empirical method for identifying possible partial saturation and determine thresholds to filter partially or fully saturated pixels in bands that are relevant to the detection and characterization of hot targets.

## II. DATA SET DESCRIPTION

In order to facilitate the analysis of saturation potential in VIIRS data, a NOAA Joint Polar Satellite System Proving Ground product named “Nightfire” is used in this study [6]. Nightfire is utilized because it contains an extensive set of prescreened “hot” pixels, allowing for fast analysis of months of data. The Nightfire algorithm selects thermally anomalous pixels detected in the VIIRS shortwave infrared (SWIR)  $1.6\text{-}\mu\text{m}$  band (M10) [6], rather than utilize the  $4\text{-}\mu\text{m}$  range that is traditionally used for fire detection [7]. VIIRS is unusual in that it records some near-infrared (NIR) and SWIR data during nighttime (bands M7, M8, and M10 in Table II), which allows for easy and rigorous detection of hot sources due to the lack

TABLE II  
SPECTRAL CHARACTERISTICS AND STATISTICS OF OBSERVED RADIANCE FOR EACH VIIRS BAND [1] IN THE NIGHTFIRE DATA SET

Band	Spectral Range ( $\mu\text{m}$ )	Central $\lambda$ ( $\mu\text{m}$ )	Specification Max <sup>1</sup>	Obs. Max <sup>1</sup>	Above Spec. Fraction <sup>2</sup> (%)	Obs. Fraction <sup>3</sup> (%)
M7	0.843 – 0.881	0.86	349	24.2	0	N/A
M8	1.225 – 1.252	1.24	165	80.3	0	N/A
M10	1.571 – 1.629	1.60	71.2	75.0	0	N/A
M12	3.598 – 3.791	3.69	353	359	0.22	0.15
M13 <sup>4</sup>	3.987 – 4.145	4.06	634	533	0	N/A
M14	8.407 – 8.748	8.58	336	349	0.002	0.0005
M15	10.234 – 11.248	10.74	343	359	0.001	0.0003
M16	11.405 – 12.322	11.86	340	356	0.001	0.0003
DNB <sup>5</sup>	0.5 – 0.9	0.7	0.0186	N/A	N/A	N/A

<sup>1</sup>Unit is  $\text{W}/\text{m}^2\text{-sr}\text{-}\mu\text{m}$  for M7, M8, M10; K for M12-M16;  $\text{W}/\text{cm}^2\text{-sr}$  for the DNB.

<sup>2</sup>Percentage of pixels above 99.9% of the design specification maximum from [1].

<sup>3</sup>Percentage of pixels above 99.9% of the observed maximum.

<sup>4</sup>Primary VIIRS fire detection band.

<sup>5</sup>The DNB has a very broad spectral range [10] and was not analyzed for saturation.

of background (solar) radiation. The nighttime background radiance at  $1.6\ \mu\text{m}$  is very low, generally of the same order of magnitude as dark current noise in the sensor. M10 is therefore selected as the primary band of Nightfire to detect thermally radiant objects, particularly gas flares with burning temperatures up to 1800 K [6]. During nighttime, pixels more radiant than the background digital count (DC) plus four standard deviations of DC are first flagged as thermally anomalous candidate pixels. The background DC is the mean DC of all nonhot pixels (DC value  $\leq 100$ ) contained in each aggregation zone for one VIIRS granule, and the standard deviation is calculated using the same criteria. To filter the noise in M10 caused by high-energy particles that frequently hit the sensor within the South Atlantic Anomaly (SAA) [3], [8] and auroral areas, the Nightfire algorithm conducts a second check on the hot pixel detected by M10 with other NIR/SWIR bands (M7 and M8) using the same technique as for M10. Finally, the algorithm attempts to fit a Planck curve to the retrieved radiances to obtain the temperature and area of the emitting source using the simplex optimization method [9]. A more thorough discussion of the Nightfire algorithm can be viewed in [6].

While Nightfire provides atmospheric-corrected data, only the uncorrected calibrated radiances for the eight M-bands (see Table II) for each pixel are examined in this study. Atmospherically-corrected data and retrieved hot spot properties are not investigated. Statistical examination of the Nightfire data (see Table II) indicates a discontinuity between data before and after March 17, 2013. Therefore, the earlier data are excluded, leaving Nightfire data from March 18, 2013 to July 14, 2013 available for use in this study. After screening out records with missing data (less than 0.01% of the data), this time period yields 1 861 865 thermally anomalous pixels. The geographic distribution of the filtered Nightfire data is shown in Fig. 2, highlighting regions of frequent biomass burning (Central Africa, Central America, Southeast Asia), as well as regions that commonly flare gas, such as the Persian Gulf, North Dakota, and Nigeria.

## III. ANALYSIS AND RESULTS

The analysis is divided into three parts. First, the nine M-bands from Table II are scrutinized by constructing

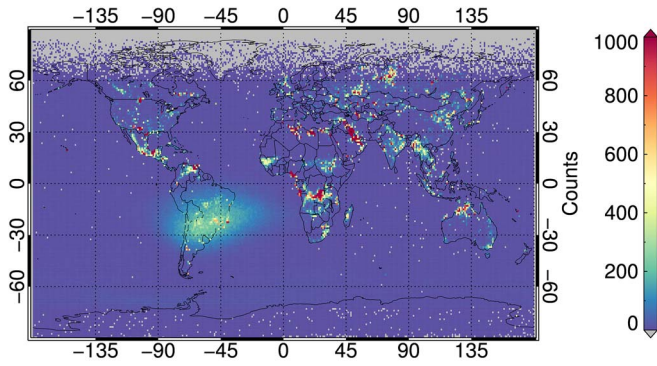


Fig. 2. Global distribution of M12 counts in the Nightfire data set, gridded to  $1^\circ \times 1^\circ$ . Clustering of counts can be observed in regions of frequent biomass burning and gas flaring. Despite Nightfire's attempts to filter it out, the blue region on and around South America still manifests as the SAA, similar to what has been observed from other sensors observing near the  $1.6\text{-}\mu\text{m}$  range [8].

histograms to identify which bands are fully saturating. Full saturation would be manifested by sudden or unexpected peaks in frequency at the highest radiance bin. Second, the most frequently saturating band's data are separated by aggregation mode to determine if there is a relationship with sample saturation and aggregation scheme. In this case, scatterplots of the data between saturating and nonsaturating bands are constructed to look for distinct populations of pixels unique to each mode. The third and final step of the analysis attempts to verify the relationship between sample saturation and aggregation by statistically simulating the effects of partial saturation. This is accomplished by using the properties of the unaggregated data (from the 1:1 aggregation zone) to generate synthetic populations of detector data that can be aggregated to match the VIIRS sample aggregation scheme and comparing the resulting histograms of the synthetic data with the observed distributions of each aggregation mode.

#### A. Band-by-Band Detection of Saturation

From the radiance histograms of each band (see Fig. 3), significant saturation is observed in the  $3.69\text{-}\mu\text{m}$  (M12) band, which is highlighted by the sudden density peak at  $3.39\text{ W/m}^2 \cdot \text{sr} \cdot \mu\text{m}$ , representing 0.15% of the data (red arrow). The approximate radiances corresponding to the theoretical limits described by [1] are indicated by the vertical dashed red lines in Fig. 3. The maximum observed radiance is slightly higher than the theoretical maximum;  $3.39\text{ W/m}^2 \cdot \text{sr} \cdot \mu\text{m}$  has a corresponding brightness temperature of  $\sim 359\text{ K}$  at the center wavelength of  $3.69\text{ }\mu\text{m}$  in comparison with the  $353\text{-K}$  brightness temperature limit reported by [1]. The incidence of partial pixel saturation as a possible side effect of aggregation is noted near 1.3, 1.8, and  $2.3\text{ W/m}^2 \cdot \text{sr} \cdot \mu\text{m}$ , which can be seen by the slight and smoothed peaks near those radiance values. Fig. 4 shows the global distribution of fully saturated ( $3.39\text{ W/m}^2 \cdot \text{sr} \cdot \mu\text{m}$ ) M12 pixels aggregated to a  $1^\circ \times 1^\circ$  grid; many of the same regions with hot spots in Fig. 2 are visible, but the SAA is notably absent.

Clustering of values near the maximum observed bins from Fig. 3 gives qualitative evidence of possible saturation in the

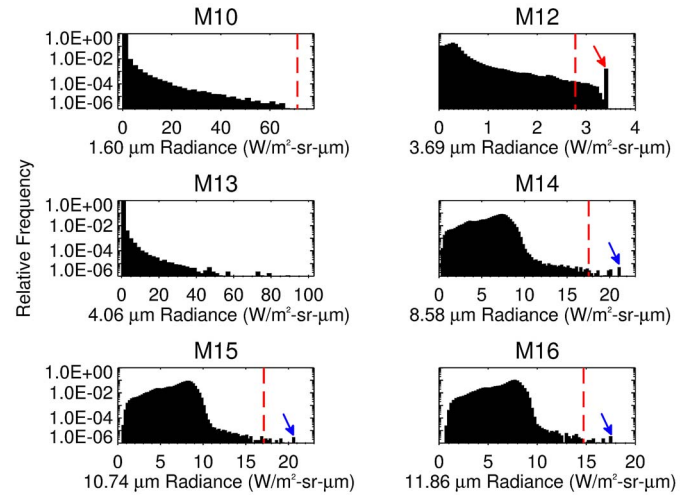


Fig. 3. Analysis of the infrared channels contained in Nightfire. The published saturation limits for each band are shown by the red dashed lines (except M13, much higher than observed data). The only channel exhibiting easily discernible saturation is M12, which has been marked with a red arrow. Blue arrows mark possible saturation features in M14, M15, and M16.

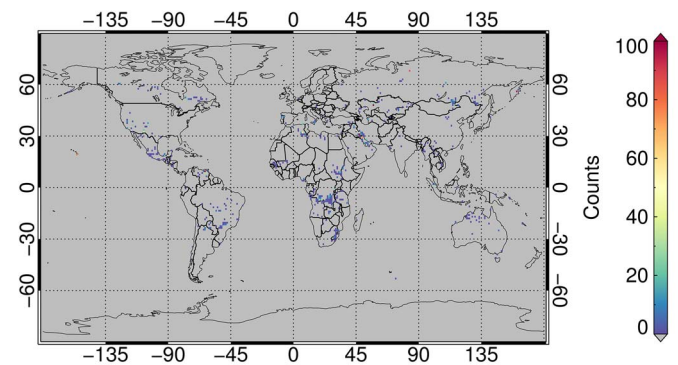


Fig. 4. Global distribution of Nightfire detections at the M12 saturation limit ( $3.39\text{ W/m}^2 \cdot \text{sr} \cdot \mu\text{m}$ ), aggregated to a  $1^\circ \times 1^\circ$  grid. Note that the color scale is an order of magnitude lower than that in Fig. 2.

M14, M15, and M16 bands (marked by the blue arrows). However, for bands other than M12, the percentage of pixels that lie above 99.9% of the nominal saturation levels and observed maximum values is very low (e.g., less than 0.002%, Table II, right columns), suggesting that saturation effects in nocturnal scenes are very rare in these bands. Bands M10 and M13 do not experience saturation in this data set.

#### B. M12 Saturation Aggregation Zone Dependence

In order to determine the effects of sample saturation in the M12 band, the data are segregated according to aggregation zone. Scatterplots of  $3.69\text{ }\mu\text{m}/4.06\text{ }\mu\text{m}$  (M12/M13) ratio versus  $4.06\text{ }\mu\text{m}$  (M13) for each aggregation zone are shown in Fig. 5. The ratio of M12/M13 is used for comparison since M13 does not saturate and lies in close spectral proximity to M12. The three panels illustrate the 1:1, 2:1, and 3:1 aggregation zones, respectively. The 1:1 pixels [see the green dots in Fig. 5 (left)] show the baseline pattern for M12, where the ratio of M12/M13 varies up to the detector saturation point of  $3.39\text{ W/m}^2 \cdot \text{sr} \cdot \mu\text{m}$ .

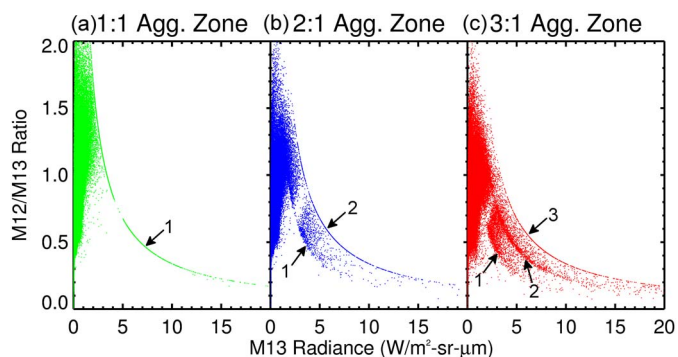


Fig. 5. Ratio of M12/M13 radiance versus M13 radiance separated by scanning angle to show the effects of onboard aggregation. (Left) 1:1 aggregation zone points ( $44.86^\circ+$ ). (Center) 2:1 aggregation zone points ( $31.72^\circ$ – $44.86^\circ$ ). (Right) 3:1 aggregation zone points ( $0^\circ$ – $31.72^\circ$ ). Aggregation results in concentrations of values along curves at lower ratios than the detector saturation limit depending on how many samples are aggregated into one pixel. These curves are overlaid with the number of samples saturating for each population.

For M13 radiances above this limit, M12/M13 is truncated, indicating that M12 is saturating while M13 is not [labeled 1 in Fig. 5 (left)]. The variability of M12/M13 at low M13 radiances shows a spread of ratios due to different thermal properties, owing to the atmospheric effects and the Planck function's sensitivity to temperature for differing wavelengths. Despite this, as the M13 radiance increases, the M12/M13 ratio converges to a curve determined by the M12 saturation limit.

The 2:1 aggregation zone [see Fig. 5 (center)] shows a similar pattern with one important and noticeable difference. As the M13 radiance increases, the M12/M13 ratio converges to two clusters with a spread of points between them. The lower cluster (labeled 1) reflects the case when one sample saturates while the other aggregated sample does not. As the ratio increases for the same M13 radiance value, there is still one saturated M12 sample, but the neighboring aggregated M12 sample is reporting increased radiances until both samples saturate (labeled 2). That is visible as the detector saturation limit of the M12/M13 ratio with the same M12 radiance of  $3.39 \text{ W/m}^2 \cdot \text{sr} \cdot \mu\text{m}$ .

Finally, in the case of the 3:1 aggregation scheme [see Fig. 5 (right)], there are three populations of curves, owing to the three samples that are averaged together. The lowest cluster represents the case when one of the aggregated M12 samples saturates (labeled 1) but the two other samples do not. The middle ratio population for a given M13 radiance is for a situation where two samples saturate but the third does not (labeled 2). Finally, the uppermost population is where all three aggregated M12 samples saturate (labeled 3).

### C. Diagnosing and Verifying New Saturation Thresholds

To confirm that these features are consistent with aggregation effects, a statistical method was devised to simulate the observed distribution of radiances in each aggregation zone. Thirty million values are randomly drawn from the observed M12 1:1 aggregation zone. The 2:1 aggregation zone is simulated by drawing 15 million random pairs from the 1:1 aggregation zone and averaging each pair, whereas the 3:1 aggregation zone is simulated by drawing 10 million triplets from the 1:1 aggregation zone and averaging them. The results of these

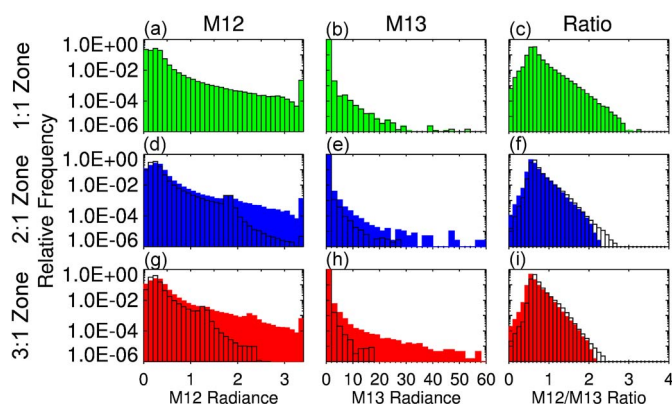


Fig. 6. Distribution of radiances (filled bars) observed and (black outlines) synthetically calculated for each aggregation zone. The three rows represent the different aggregation modes starting with 1:1 at the top and ending with 3:1 at the bottom, whereas the three columns are M12 radiance, M13 radiance, and M12/M13 ratios, from left to right. Solid bars represent the observed distributions of radiances, and the black outlines represent the synthetic distributions made by averaging samples drawn from the edge scan data set (see Section III-C for details).

simulations are displayed in Fig. 6, which is divided into nine panels. In each panel, the colored bars show the observed distribution from the Nightfire data, and the black lines show the statistically created distributions. The three rows represent the aggregation zones starting with 1:1 at the top and ending with 3:1 at the bottom, whereas the three columns are  $3.69\text{-}\mu\text{m}$  radiance (M12),  $4.06\text{-}\mu\text{m}$  radiance (M13), and  $3.69/4.06 \mu\text{m}$  ratios (M12/M13), respectively, from left to right. The statistically simulated radiance values almost exactly reproduce the observed distributions of radiances from the 1:1 aggregation zone (see the top row in Fig. 6). The randomly selected pairs and triplets (see the second and third rows in Fig. 6) show peaks of density in the same locations as the observed data, indicating the effects of saturation well below the detector saturation limit.

Saturation can be seen to affect radiances as low as  $1.7 \text{ W/m}^2 \cdot \text{sr} \cdot \mu\text{m}$  ( $\sim 337 \text{ K}$  at  $3.69 \mu\text{m}$ ) for the 2:1 aggregation zone [see Fig. 6(d)]. In the 3:1 aggregation zone, the influence of an individual saturated sample becomes apparent at radiances of only  $1.3 \text{ W/m}^2 \cdot \text{sr} \cdot \mu\text{m}$  ( $\sim 330 \text{ K}$ ). The second column shows the observed and synthetic distributions for the M13 ( $4.06 \mu\text{m}$ ) band, where no unusual peaks in density are noted. The far right column shows suppression of high values of M12/M13 with aggregation, consistent with the effects of averaging. The geographic distribution of potential partially saturated pixels is displayed in Fig. 7, where data are mapped only if the radiance values reach above the thresholds of possible partial saturation ( $1.3 \text{ W/m}^2 \cdot \text{sr} \cdot \mu\text{m}$  for 3:1 aggregation,  $1.7 \text{ W/m}^2 \cdot \text{sr} \cdot \mu\text{m}$  for 2:1 aggregation, and  $3.39 \text{ W/m}^2 \cdot \text{sr} \cdot \mu\text{m}$  for 1:1 aggregation). In comparison with the observed detector saturation limit (see Fig. 4), a much larger area is impacted by partial saturation.

While the general pattern of the observed and simulated distributions is similar, particularly the features caused by detector saturation, large discrepancies exist. One main difference stems from sample correlation. Normally, when VIIRS scans a scene, adjacent samples will observe a similar environment;

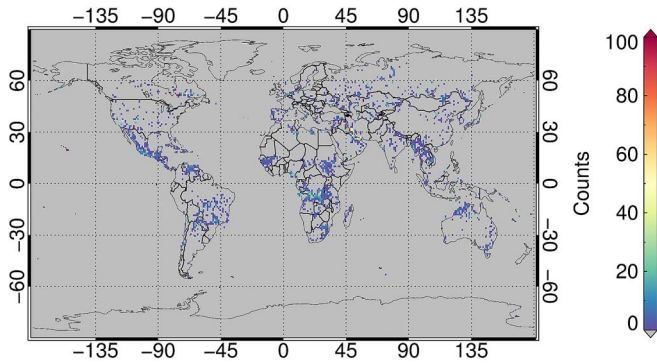


Fig. 7. Global distribution of the partially saturated M12 pixel counts to a  $1^\circ \times 1^\circ$  grid. Partial saturation is determined by taking the lowest temperature at which saturation artifacts are observed in each aggregation zone. The color scale is the same as that in Fig. 4.

that is, if one sample scans a fire, the chances are high that the adjacent sample(s) will also scan hot terrain. This greatly increases the frequency of high temperatures occurring in the observations compared with randomly selected samples. Another compounding factor is the difference in IFOV, which is dependent on scan angle. While the pixel footprint change is reduced by aggregation, detector footprint sizes for VIIRS still increase significantly with scan angle. Thus, the detector IFOV near nadir is much smaller than at the scan edge, which leads to higher fire fractions and, subsequently, increased occurrence of very high radiances in the near-nadir samples when compared with the 1:1 aggregation zone samples. These two effects have similar impacts on the observed distribution; therefore, they cannot be easily separated for analysis or considered in the simulated distributions. This demonstrates that extrapolation from the 1:1 zone tends to underestimate the occurrence of saturation in the 2:1 and 3:1 aggregation regimes.

#### IV. SUMMARY AND CONCLUSION

This letter investigated the prevalence and influence of detector saturation when the VIIRS sample aggregation scheme is applied. It should be noted that saturation may occur more frequently than the Nightfire data set indicates because fires tend to burn hotter in the daytime than at night. The only band to suffer from significant deleterious detector saturation is the  $3.69\text{-}\mu\text{m}$  band (M12), but there is some evidence to support saturation in the other single-gain thermal infrared (TIR) channels that might be more apparent in a larger data set. The maximum radiance values recorded by VIIRS in those bands are significantly higher than the published maxima in [1]. For the M12 band, distinct clustering of pixel radiances below the detector saturation limit of  $3.39\text{ W/m}^2 \cdot \text{sr} \cdot \mu\text{m}$  ( $\sim 359\text{ K}$ ) appears in the data from the 2:1 and 3:1 aggregation zones. The 1:1 aggregation zone's saturation limit is thus  $3.39\text{ W/m}^2 \cdot \text{sr} \cdot \mu\text{m}$  ( $\sim 359\text{ K}$ ), whereas the 2:1 aggregation

zone exhibits saturation at  $1.7\text{ W/m}^2 \cdot \text{sr} \cdot \mu\text{m}$  ( $\sim 337\text{ K}$ ), and the 3:1 aggregation zone is susceptible to saturation only at  $1.3\text{ W/m}^2 \cdot \text{sr} \cdot \mu\text{m}$  ( $\sim 330\text{ K}$ ).

VIIRS does not record when saturation occurs in individual samples. Therefore, it is impossible to know if a pixel is affected by saturation in the M12 band beyond its respective saturation threshold. The potential for biases in pixel radiance due to unidentified saturation is a significant problem for quantitative use of the M12 band for applications that use hot pixels, such as for multispectral fire property retrievals. M12's intended use for sea surface temperature derivation [1], [11] should not be impacted, provided pixels are filtered to avoid hot sources such as gas flaring. For applications that require quantitative evaluation of hot sources, the aggregation scheme determines the upper limit of radiances known to be unsaturated.

#### ACKNOWLEDGMENT

The Nightfire data used for this letter can be obtained at [http://ngdc.noaa.gov/eog/viirs/download\\_viirs\\_fire.html](http://ngdc.noaa.gov/eog/viirs/download_viirs_fire.html). The authors would like to thank the Naval Research Enterprise Internship Program for the opportunity for T. Polivka to be an Intern at the Naval Research Laboratory (NRL), Monterey, CA, USA, and the staff at NRL for their advice and suggestions. They would also like to thank the group of C. Elvidge for their work on Nightfire.

#### REFERENCES

- [1] C. Cao, F. J. De Luccia, X. Xiong, R. Wolfe, and F. Weng, "Early on-orbit performance of the visible infrared imaging radiometer suite onboard the Suomi National Polar-Orbiting Partnership (S-NPP) Satellite," *IEEE Trans. Geosci. Remote Sens.*, vol. 52, no. 2, pp. 1142–1156, Feb. 2014.
- [2] R. E. Wolfe *et al.*, "Suomi NPP VIIRS prelaunch and on-orbit geometric calibration and characterization," *J. Geophys. Res.—Atmos.*, vol. 118, no. 20, pp. 11 508–11 521, Oct. 2013.
- [3] W. Schroeder, P. Oliva, L. Giglio, and I. A. Csizsar, "The New VIIRS 375 m active fire detection data product: Algorithm description and initial assessment," *Remote Sens. Environ.*, vol. 143, pp. 85–96, Mar. 2014.
- [4] I. Csizsar *et al.*, "Active fires from the Suomi NPP visible infrared imaging radiometer suite: Product status and first evaluation results," *J. Geophys. Res.—Atmos.*, vol. 119, no. 2, pp. 803–816, Jan. 2014.
- [5] D. Hillger *et al.*, "First-light imagery from Suomi NPP VIIRS," *Bull. Amer. Meteorol. Soc.*, vol. 94, no. 7, pp. 1019–1029, Jul. 2013.
- [6] C. D. Elvidge, M. Zhizhin, F. Hsu, and K. E. Baugh, "VIIRS nightfire: Satellite pyrometry at night," *Remote Sens.*, vol. 5, no. 9, pp. 4423–4449, Sep. 2013.
- [7] D. Peterson, J. Wang, C. Ichoku, E. Hyer, and V. Ambrosia, "A sub-pixel-based calculation of fire radiative power from MODIS observations: 1 Algorithm development and initial assessment," *Remote Sens. Environ.*, vol. 129, pp. 262–279, Feb. 2013.
- [8] S. Casadio and O. Arino, "Monitoring the south atlantic anomaly using ATSR instrument series," *Adv. Space Res.*, vol. 48, no. 6, pp. 1056–1066, Sep. 2011.
- [9] J. Lagarias, J. Reeds, M. Wright, and P. Wright, "Convergence properties of the Nelder–Mead simplex method in low dimensions," *SIAM J. Optim.*, vol. 9, no. 1, pp. 112–147, Dec. 1998.
- [10] L. B. Liao, S. Weiss, S. Mills, and B. Hauss, "Suomi NPP VIIRS day-night band on-orbit performance," *J. Geophys. Res.—Atmos.*, vol. 118, no. 22, pp. 12705–12718, Nov. 2013.
- [11] T. E. Lee *et al.*, "The NPOESS VIIRS day/night visible sensor," *Bull. Amer. Meteorol. Soc.*, vol. 87, no. 2, pp. 191–199, Feb. 2006.